



# 1

## Thermoelectric Power Generators and Their Applications

Jianxu Shi and Ke Wang

*School of Automation, Xi'an University of Posts & Telecommunications, Xi'an, 710121, China*

### 1.1 Introduction

Energy is a fundamental requirement for the development of human society. In recent decades, the rapid increase in energy demand has led to the emergence of an energy crisis. Moreover, in the industrial production process, the majority of energy is wasted in the form of heat, which further exacerbates this crisis. Therefore, knowing how to convert these waste heat into effective electrical energy is beneficial to solving current energy problems. Thermoelectric conversion technology, achieving the conversion between heat or temperature gradients and electrical energy, may be a promising strategy. Thermoelectric conversion technology covers multiple stages, including material preparation, materials forming, device fabrication, and system integration. Among them, thermoelectric materials are the basis, while thermoelectric devices are the core that allows the leap from thermoelectric materials to thermoelectric conversion technology. Meantime, device design and fabrication covers such interdisciplinary scientific and technological issues as thermodynamics, thermal processing, interface physics and engineering, and reliability design.

In this section, we introduce the principle of thermal conversion technology, then discuss various thermoelectric materials, the preparation and forming of thermoelectric materials, and multifunctional thermoelectric devices. Finally, a conclusion and insightful outlook is given. Here, we present the advanced understanding of thermoelectric materials and some new-type preparation and forming methods, which can provide new opportunities for the further advancement of thermoelectric conversion technology in a wide variety of applications.

### 1.2 Principles of Thermoelectric Conversion

#### 1.2.1 Seebeck Effect

In 1823, Thomas Seebeck discovered that the compass pointer would slowly deflect when it was placed near a circuit composed of two different metals with a temperature gradient. This is the first observation of the phenomenon of electricity

*Renewable Energy Technologies for Low-Carbon Development*, First Edition.

Edited by Chunbao Du, Yuan Cheng, and Gang Zhang.

© 2025 WILEY-VCH GmbH. Published 2025 by WILEY-VCH GmbH.



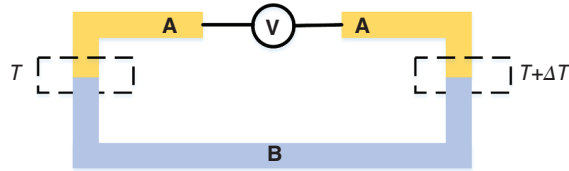


**Figure 1.1** Diagram of the Seebeck effect.

induced by temperature difference. Subsequently, he implemented comparative studies on various metals, and identified the existence of electromotance induced by temperature difference, which provides the fundamental principle for sensing temperature using thermocoupling. To commemorate his contributions, this phenomenon is called the Seebeck effect (Figure 1.1). With the Seebeck effect, the circuit is composed of two metals, A and B. In this circuit, metals A and B come into contact to form two nodes. Interestingly, there is a temperature difference  $\Delta T$  between these two nodes, and then an electrical potential difference between the two nodes can be detected by a voltmeter connected in the circuit. With this effect, the generated thermoelectric electromotance has two fundamental properties: (i) the thermoelectric electromotance is only related to the temperature difference between the two nodes and does not rely on the temperature of the wire between the two nodes; (ii) the electromotance formed by the contact between conductors A and B, is independent of whether a third metal, C, is connected between the two nodes. These two fundamental properties render the wide application of the Seebeck effect in wearable devices, wireless sensor networks, and the aerospace field [1].

### 1.2.2 Peltier Effect

Twelve years after the Seebeck effect was discovered, another fantastic thermoelectric phenomenon was observed by Peltier (Figure 1.2). It can be found that the contact junction in the circuit will suffer endothermic or exothermic experience, after powering on the circuit composed of two conductors, A and B. Considering that conductors A and B have different electron concentrations and the Fermi level, the contact between conductors A and B will cause unequal electron diffusion at the junction, resulting in the establishment of an electric field between the two metals at the junction, thus establishing the electrical potential difference. This

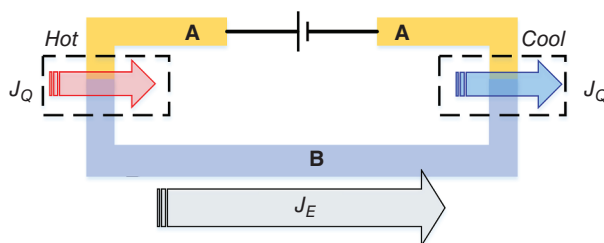


**Figure 1.2** Diagram of the Peltier effect.

thermoelectric phenomenon is called the Peltier effect, which is the foundation of thermoelectric refrigeration. The Peltier electrical potential difference is a function of temperature, and the dependence of the Peltier electrical potential difference on temperature also varies for different junctions. When the current is reversed, the endothermic or exothermic behaviors of two junctions would also be reversed, thus it is suggested that the direction of heat flux ( $JQ$ ) is dependent on the electrical current ( $JE$ ) flow. After hundreds of years of research in thermoelectric materials, it is well known that if current flows from N-type materials to P-type materials, carriers will conduct away the thermal energy and reduce temperature, thereby cooling the junction. Conversely, if electrical current flows from the P-type conductor material into the N-type conductor material, the temperature of the junction will increase. The relationship between the thermal energy ( $Q$ ) and electrical current ( $I$ ) is  $dQ/dt = \Pi I$  with the Peltier coefficient ( $\Pi$ ), suggesting that the rate of heat generation is directly proportional to the intensity of the electrical current passed through the junction. The Peltier electrical potential of general metal junctions is  $\mu\text{V}$  level, while semiconductor junctions can be several orders of magnitude larger than it.

### 1.2.3 Thomson Effect

In 1851, W. Thomson derived the relationship between the Seebeck coefficient ( $S$ ) and Peltier coefficient ( $\Pi$ ):  $S = \Pi/T$ , and predicted that there should be a third thermoelectric phenomenon based on the thermodynamics. If a current goes across a uniform conductor with a certain temperature gradient, in addition to generating irreversible Joule heat, the conductor would also absorb or release amounts of heat. This phenomenon is called the Thomson effect, and the heat absorbed or released is called Thomson heat. Unlike the Seebeck and Peltier effects, the Thomson effect acts on the same conductor. Assuming the electrical current flows through a uniform conductor  $I$ , there will be a corresponding temperature difference ( $\Delta T$ ) in the direction of the electrical current. So the endothermic rate of the electrical current on this conductor can be written as  $dQ/dt = \beta I \Delta T$  with the Thomson coefficient ( $\beta$ ). Subsequently, W. Thomson derived the relationship between the Seebeck coefficient ( $S$ ), Peltier coefficient ( $\Pi$ ), and Thomson coefficient ( $\beta$ ) using the theoretical approximation of balanced forces:

$$S_{ab} = \Pi_{ab}/\Delta T, \quad dS_{ab}/dT = (\beta_a - \beta_b). \quad (1.1)$$

Thomson heat is also reversible, but it is difficult to measure the Thomson heat experimentally, due to the difficulty of distinguishing Thomson heat from Joule heat.

### 1.2.4 Evaluation Indicators for Thermoelectric Materials and Devices

In 1911, Altenkirch proposed a theoretical expression for the figure of merit ( $ZT$ ) of thermoelectric materials, which is as follows [2, 3]:

$$ZT = \frac{S^2 \sigma}{k} T = \frac{S^2 \sigma}{k_C + k_L + k_B} T \quad (1.2)$$

where  $S$ ,  $\sigma$ , and  $k$  are the Seebeck coefficient, electrical conductivity, and thermal conductivity of thermoelectric materials, respectively. The thermal conductivity is contributed by the carriers ( $k_C$  and  $k_B$ ) and lattice vibration. Meantime, the multiple of  $S$  and  $\sigma^2$  is called the power factor. From Eq. (1.2), it is known that the value of  $ZT$  varies with temperature for a thermoelectric materials, and the value of  $ZT$  is proportional to the power factor but inversely proportional to the thermal conductivity of the material. To obtain high-performance thermoelectric materials, i.e. thermoelectric materials with high  $ZT$ , the materials should have high conductivity and a large Seebeck coefficient. High conductivity can reduce the heat loss caused by Joule heat, and a large Seebeck coefficient ensures the large electromotance of thermoelectric materials under specific temperature gradients. In addition, the low thermal conductivity is beneficial for maintaining the temperature gradient.

For a thermoelectric device, its maximum conversion efficiency ( $\eta_{\max}$ ) is determined by the efficiency of the Carnot cycle and the  $ZT$  value of thermoelectric materials [4], as follows:

$$\eta_{\max} = \eta_{\text{Carnot}} \times \eta_{\text{Materials}} = \frac{T_H - T_C}{T_H} \times \frac{\sqrt{1 + ZT} - 1}{\sqrt{1 + ZT} + T_C/T_H}. \quad (1.3)$$

From Eq. (1.3), we can find the maximum conversion efficiency of thermoelectric devices increases with the increase of  $ZT$  and temperature difference. Therefore, increasing the value of  $ZT$  is useful for improving the maximum thermoelectric conversion efficiency of thermoelectric devices.

## 1.3 Thermoelectric Materials

### 1.3.1 Traditional Thermoelectric Materials

**GeTe material:** GeTe is an extensively used thermoelectric material for working in the mid-temperature range. GeTe is a semiconductor with a narrow band gap and large hole carrier concentration of  $\sim 10^{21} \text{ cm}^{-3}$  [5]. When the temperature increases over approximately 600–700 K, GeTe undergoes a phase transition from rhombohedral structure (R-GeTe) with lattice parameters of  $a = 4.156 \text{ \AA}$  and  $c = 10.663 \text{ \AA}$  and the space group of R3m to cubic structure (C-GeTe) with a lattice parameter of  $a = 5.996 \text{ \AA}$  and the space group of Fm $\bar{3}$ m (Figure 1.3a–d) [6]. In Figure 1.3e, the photograph of  $(\text{GeTe})_x(\text{AgSbTe}_2)_{100-x}$  (commonly called TAGS- $x$ ) pellets is presented, which was prepared by gas-atomization followed by spark plasma sintering (SPS) [7]. The temperature-dependent  $ZT$  and average  $ZT$  ( $zT_{\text{avg}}$ ) of the GeTe family materials have been studied in a large temperature region (Figure 1.3f,g) [8]. To achieve an ultralow lattice thermal conductivity, high-entropy engineering for thermoelectrics is one of the latest promising strategies. The large strains can be caused in high entropy materials due to the severely distorted lattices, which strengthens the phonon scattering and reduced lattice thermal conductivity significantly [9]. He and coworkers [10] have improved the  $ZT$  value of GeTe to 2.7 at 750 K using the high-entropy engineering.

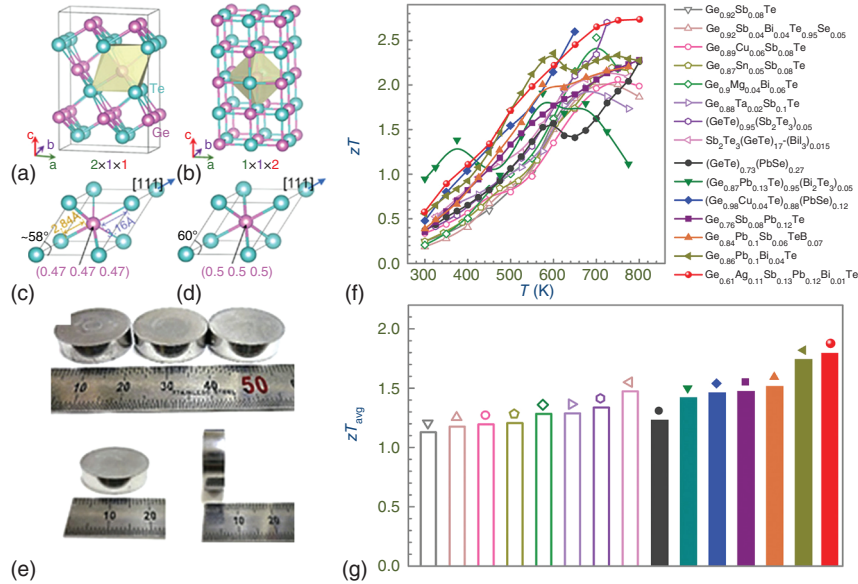


**Figure 1.3** GeTe thermoelectric features. Crystal structures of R-GeTe (a) and C-GeTe (b) as well as the corresponding primitive cells of R-GeTe (c) and C-GeTe (d). Source: Hong et al. [6]/Reproduced with permission from John Wiley & Sons. (e) Photograph of  $(\text{GeTe})_x(\text{AgSbTe}_2)_{100-x}$  (commonly called TAGS-x) pellets prepared by gas-atomization (GA) plus spark plasma sintering (SPS). Source: Reproduced with permission from Kim et al. [7]/ELSEVIER. (f) Representative temperature-dependent  $zT$ , and (g) the average value of  $zT$  ( $zT_{\text{avg}}$ ). Source: Hong et al. [8]/John Wiley & Sons/CC BY 4.0.

**$\text{Bi}_2\text{Te}_3$  material:** Since 1954, Goldsmid firstly proposed and verified bismuth telluride ( $\text{Bi}_2\text{Te}_3$ ) as potential thermoelectric materials [11].  $\text{Bi}_2\text{Te}_3$  is a semiconductor material with the highest thermoelectric performance at room temperature, and it has been commercially produced. Therefore,  $\text{Bi}_2\text{Te}_3$  has become one of the most developed and most frequently used thermoelectric materials, and its binary crystal structure belongs to triangular crystal systems. Bi atoms and Te atoms are along the crystallographic  $c$ -axis, forming  $\text{Te}^{(1)}\text{-Bi-Te}^{(2)}\text{-Bi-Te}^{(1)}$  five atomic sublayers (Figure 1.4a). Meantime, these atomic layers are alternately arranged and stacked to form a hexagonal layered structure.  $\text{Te}^{(1)}$  and Bi atoms are bonded by both the covalent bond and ionic bond, while  $\text{Te}^{(2)}$  and Bi atom are bonded only by the covalent bond. There is the non-bond Van der Waals coupling between adjacent  $\text{Te}^{(1)}$  and  $\text{Te}^{(1)}$  sublayers. In  $\text{Bi}_2\text{Te}_3$  compound, the ionic covalent bonds are the strongest, while the van der Waals coupling is the weakest. Therefore,  $\text{Bi}_2\text{Te}_3$  alloys are prone to slip in the  $\text{Te}^{(1)}\text{-Te}^{(1)}$  layer and dissociate perpendicular to the  $c$ -axis. Hence, the dimension of  $\text{Bi}_2\text{Te}_3$  can be decreased to two dimensionl (2D). At present, The single crystal of  $\text{Bi}_2\text{Te}_3$  compound is common, and can be cleaved (Figure 1.4b,c) [12]. According to the stoichiometric ratio of  $\text{Bi}_2\text{Te}_3$ , the alloy prepared by meltinod or zon- melting method exhibits p-type conductivity. Because elemental Te has a high saturated vapor pressure, and it is volatize during the melting process, this resung in a large number of Te vacancies in the  $\text{Bi}_2\text{Te}_3$

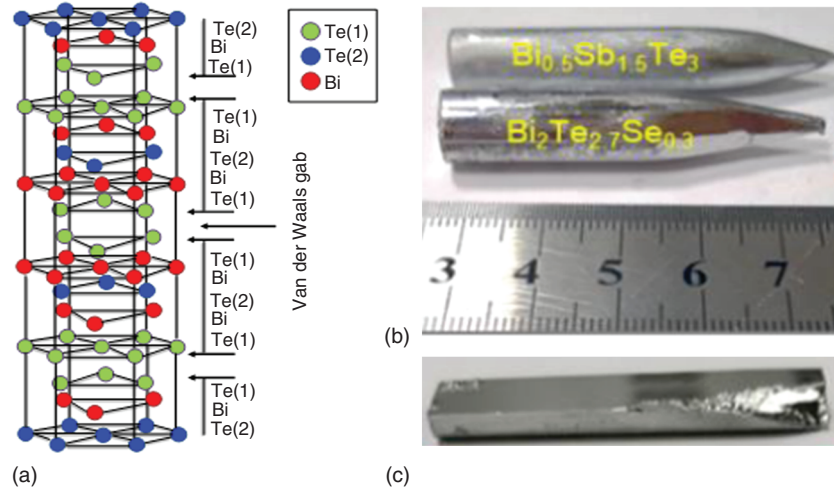


**Figure 1.4** (a) Crystal structures of Bi<sub>2</sub>Te<sub>3</sub> crystal. Photo image of the single Bi<sub>2</sub>Te<sub>3</sub> single crystal (b) and cleavage surface (c) after dissociation. Source: Reproduced with permission from Lu et al. [12]/Springer Nature.

compound. Subsequently, Bi occupies the Te vacancies to form antisite defects, which increases the hole concentration, resulting in p-type conduction. The lattice parameters of Bi<sub>2</sub>Te<sub>3</sub> are  $a = 4.395 \text{ \AA}$  and  $c = 30.44 \text{ \AA}$ . The band gap of Bi<sub>2</sub>Te<sub>3</sub> is  $\sim 0.13 \text{ eV}$  at room temperature, and its molar mass, density and melting point are  $800.76 \text{ g mol}^{-1}$ ,  $7.74 \text{ g cm}^{-3}$ , and  $580 \text{ }^\circ\text{C}$ , respectively. In order to improve the thermoelectric properties of Bi<sub>2</sub>Te<sub>3</sub> doping can be employed. For instance, p-type Bi<sub>2-x</sub>Sb<sub>x</sub>Te<sub>3</sub> can be formed by the doping of Sb element, and n-type Bi<sub>2-x</sub>Se<sub>x</sub>Te<sub>3</sub> is formed by Se element doping. Meantime, the lattice thermal conductivity of bismuth telluride can be reduced by nanostructure, which is also useful to improve the thermoelectric performance of Bi<sub>2</sub>Te<sub>3</sub> compounds [13].

### 1.3.2 Half-Heusler Alloys

Half-Heusler alloys have attracted extensive attention, due to their stable chemical, good mechanical, and excellent thermoelectric properties in the medium and high temperature range (700–1000 K). Half-Heusler alloys can be represented by the general formula ABC, where A is the most electronegative transition element, such as Zr, Hf, Ti, V, Nb, etc., and B is a weaker electronegativity transition element, such as Ni, Co, Fe, etc., and C is the main group element, such as Sn, Sb element (Figure 1.5a) [14–17]. Lattice thermal conductivities of major half-Heusler thermoelectric materials are comparable to other common thermoelectric materials (Figure 1.5b) [18]. Meanwhile, the thermoelectric performance of half-Heusler alloys can also be evaluated by the band-structure manipulation, and the band engineering can be achieved by the point defect and substitution doping. Li et al. [19] improved the performance of FeNbSb-based half-Heusler alloys by band manipulation, and they found the band structure of FeNbSb-based half-Heusler alloys displays high band degeneracy near



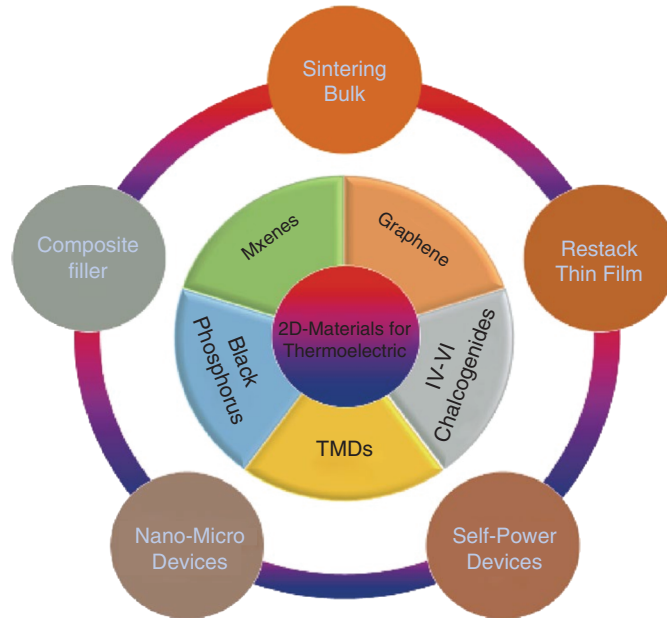


**Figure 1.6** Two-dimensional (2D) materials for thermoelectric conversion. Source: Li et al. [20]/Springer Nature/CC BY 4.0.

maximum (up to  $8.5 \text{ mW} [\text{m}^{-1} \cdot \text{K}^{-1}]$ ) at bilayer  $\text{MoS}_2$  while the Seebeck coefficient is insensitive to the number of layers. Besides, other TMDs also have giant potential in thermoelectric conversion, because the thermal conductivity of TMDs can be manipulated effectively by the type of chalcogen [27]. It has been identified by theoretical and experimental studies that the thermal conductivity of TMDs shows a reduction when the type of chalcogen changes from S to Se, which is useful for thermoelectric conversion.

Compared to TMDs, the band gap of black phosphorus can be tailored over a wider range (0.3–2.0 eV) by controlling the number of layers [28]. Due to the corrugated geometrical structure of black phosphorus, as well as its electrical, phononic, mechanical, and thermal properties, it behaves strong in-plane anisotropy between the armchair (AC) and zigzag (ZZ) directions. In the AC direction, black phosphorus shows stronger anharmonicity, lower group velocity, and phonon relaxation time than in the ZZ direction [29, 30], resulting in the anisotropic ratio of thermal conductivity between the ZZ and AC direction of up to 2.2 times [31]. Interestingly, the anisotropy of electronic properties is opposite to that of thermal conductivity in black phosphorus [32]. In the AC direction with lower thermal conductivity, higher conductivity and Seebeck coefficient occur. This phenomenon that better electrical performance and lower thermal performance occur in the same direction meets the demand for high thermoelectric figures of merit. SnSe is one of IV-VI chalcogenides, whose structure is similar to black phosphorus. 2D SnSe has strong anisotropy and anharmonicity due to the unequivalent occupations of Sn and Se atoms in its geometrical structure, which is reflected in the large Grüneisen constants. These large

Grüneisen constants result in the extremely low thermal conductivity of 2D SnSe, which is beneficial for thermoelectric applications [33–36]. MXene, a new group of 2D materials, is defined as  $M_{n+1}AX_n$ , where M represents the early transition metal, while A and X are the element from groups 13–16 in the periodic table and the carbon/nitrogen atoms, respectively. The value of  $n$  can be 1, 2, or 3. The electronic properties of MXene can be tuned between metallic, semiconducting, and half-metallic states by surface functionalization. Unlike black phosphorus prone to oxidation in the air, MXene possesses excellent thermal stability, and is thus often studied for the high-temperature thermoelectric conversion. In 2014, Khazaei et al. [37] predicted the thermoelectric properties of more than 35 functionalized MXene monolayers through first-principles calculations, and proved that monolayer and multilayer  $Mo_2C$  exhibit a higher power factor than other MXenes. Subsequently, Kim et al. [38] fabricated two kinds of  $Mo_2C$ -based MXene flexible thin films, and discovered the power factor of  $Mo_2TiC_2T_x$  film is up to  $309 \mu W m K^{-2}$  at 800 K, making this promising for thermoelectric conversion at high temperatures.

2D materials are more sensitive to the surface and geometrical structure than bulk materials, thus the electronic, thermal and thermoelectric properties can be manipulated effectively by doping [39], defect [40, 41], strain [42, 43] and heterostructure [44, 45]. For instance, the thermal conductivity of graphene is measured at about  $5000 W (m^{-1} \cdot K^{-1})$  by Balandin [46, 47], which is detrimental for thermoelectric conversion. In 2011, Seol et al. [48] placed the graphene on  $SiO_2$  substrate and found the thermal conductivity decreased to  $500\text{--}600 W (m^{-1} \cdot K^{-1})$  at room temperature. This is mainly due to the interaction between acoustic phonons and the substrate, which greatly suppresses the contribution of acoustic phonons to thermal conductivity, resulting in a lower thermal conductivity than suspended graphene. Besides, there is still a long way to go for the practical applications of 2D materials in thermoelectric conversion. Because it is still difficult to prepare 2D semiconductor materials with high mobility on a large scale. Furthermore, complex devices need to be made when measuring the thermoelectric properties of 2D semiconductor materials, which would introduce more defects and other uncertainties and make it challenging to measure the intrinsic properties of 2D materials.

#### 1.3.4 Thermoelectric Liquid Materials

Thermoelectric liquid materials mainly contain two types, one is slurry and another is ink (Figure 1.7). In 2015, He et al. [49] firstly reported p-type  $Bi_{0.5}Sb_{1.5}Te_3$  (BST) slurry and its photoresins (Figure 1.7a). This slurry was used as 3D printing (sterolithography apparatus, SLA) raw materials, and the printed sample exhibited excellent thermal performance. Compared to thermoelectric slurries, inks have a lower viscosity. The single-crystalline  $Bi_2Te_3$  thermoelectric nanowires (BTNWs) are dispersed in deionized (DI) water (Figure 1.7b), and formed inkjet-printed BTNWs. These inkjet-printed BTNWs provide good thermoelectric performances as their Seebeck coefficient reached up to  $140 \mu V K^{-1}$  [50]. The BiSbTe-based all-inorganic inks can be formulated by dispersing  $Bi_xSb_{2-x}Te_3$  micro-particles in the presence of  $Sb_2Te_4$  as an inorganic binder in glycerol [51] (Figure 1.7c). The

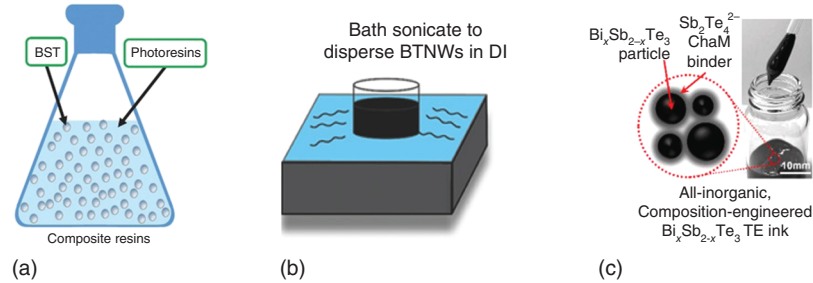


**Figure 1.7** Images of  $\text{Bi}_{0.5}\text{Sb}_{1.5}\text{Te}_3$  (BST) particle in photoresin (a),  $\text{Bi}_2\text{Te}_3$  nanowire in deionized water (b), as well as the images of all-inorganic (c). Sources: (a) Reproduced with permission from He et al. [49]/John Wiley and Sons. (b) Reproduced with permission from Chen et al. [50]/with permission John Wiley & Sons. (c) Reproduced with permission from Yang et al. [51]/ELSEVIER.

$\text{Bi}_2\text{Te}_3$ -based inorganic paints were prepared by employing the molecular  $\text{Sb}_2\text{Te}_3$  chalcogenidometalate as a sintered precursor, and possessed  $ZT$  values of 0.67 and 1.21 for n- and p-type painted materials [52], respectively. The all-inorganic viscoelastic  $\text{Bi}_2\text{Te}_3$ -based inks were synthesized by using chalcogenidometalate ions as inorganic binders [53], while the single-crystal nanoplates  $\text{Bi}_2\text{Te}_{2.8}\text{Se}_{0.2}$  were mixed in solvent ( $\alpha$ -Terpineol) using a planetary centrifugal mixer for a uniform mixture.

## 1.4 Preparation of Thermoelectric Materials

Generally, thermoelectric materials can be prepared by the Bridgman method, melting, mechanical alloying, solvothermal synthesis, and printing alloying. A schematic diagram of the Bridgman method is given (Figure 1.8a), which has been widely used in the preparation of thermoelectric single crystals [54]. SnSe has attracted widespread interest, due to its outstanding thermoelectric performance. By substituting Bi at Sn sites, successful synthesis of n-type SnSe single crystals was achieved by the temperature gradient growth method. At 773 K, the highly doped n-type SnSe with carrier density of  $-2.1 \times 10^{19} \text{ cm}^{-3}$  reached the maximum  $ZT$  value of 2.2 along the  $b$ -axis [55] (Figure 1.8b). The single crystal p-type  $\text{Bi}_{0.5}\text{Sb}_{1.5}\text{Te}_3$  and n-type  $\text{Bi}_2\text{Te}_{2.7}\text{Se}_{0.3}$  are synthesized by zone melting and the Bridgman technique with a three-temperature-zone furnace. Then, the films are exfoliated from the corresponding single crystal. The power factors of p-type and n-type are 42 and  $46 \mu\text{W cm}^{-1} \text{ K}^{-1}$  [12] (Figure 1.8c). Layered materials based on  $\text{Mg}_3\text{Bi}_2$ , composed of non-toxic and abundantly available elements, are being widely regarded as a highly promising option for thermoelectric applications. Besides, single crystals of  $\text{Mg}_3\text{Bi}_2$ -based materials with high quality and precise compositional control are grown using the Bridgman method [56] (Figure 1.8d).

Currently, the most prevalent and widely adopted method to prepare thermoelectric materials is the melting process, due to its high productivity, easy operation, and

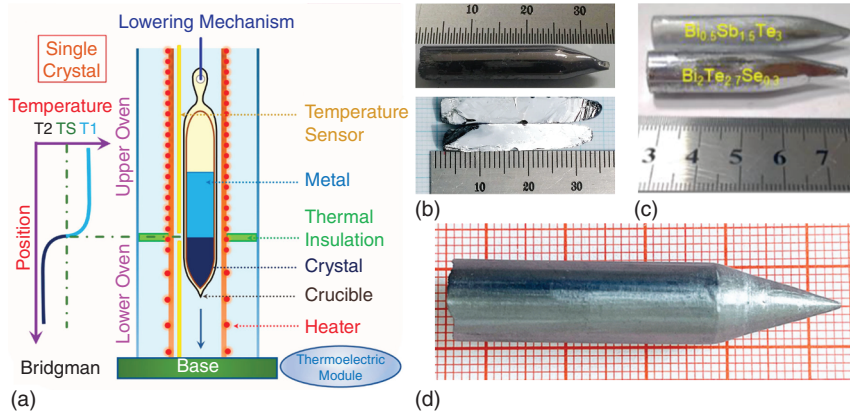


**Figure 1.8** (a) Schematic diagram of the Bridgman method. Pictures of SnSe (b),  $\text{Bi}_2\text{Te}_3$  (c),  $\text{Mg}_3\text{Bi}_2$  (d) single crystal. Sources: (a) Reproduced with permission from Shi et al. [54]/American Chemical Society. (b) Duong et al. [55]/Springer Nature/CC BY 4.0. (c) Reproduced with permission from Shi et al. [54]/American Chemical Society. (d) Reproduced with permission from et al. [56]/ ELSEVIER.

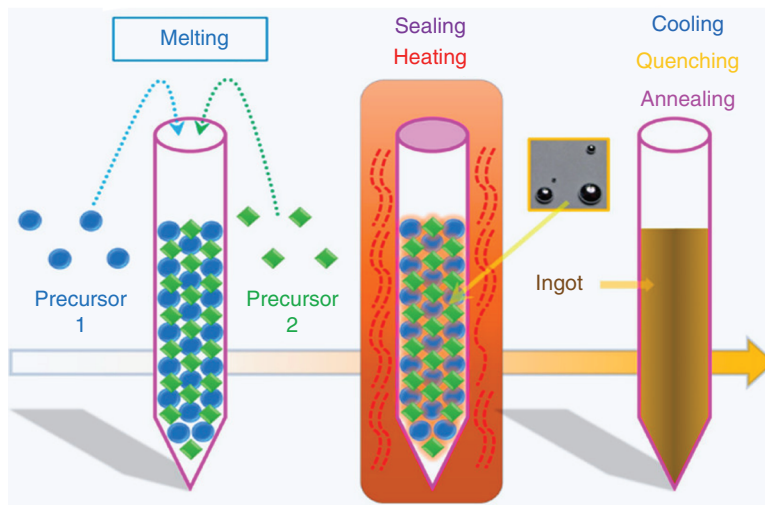


**Figure 1.9** Schematic diagram of the melting method. Source: Reproduced with permission from Shi et al. [54]/American Chemical Society.

affordable characteristic. The schematic diagram and basics of the melting process are given (Figure 1.9). This process mainly involves three stages: (i) heating the high-purity precursors above their melt points in a quartz tube; (ii) keeping the high-purity precursors at high temperature for an appropriate time; (iii) cooling to the room temperature slowly. At present, the SnSe ingot [57],  $\text{Bi}_2\text{Te}_3$  alloys [58], and TiNiSn half-Heusler alloys [59] have been fabricated by this melting process. However, there is a disadvantage to this method that it is difficult to control the structures and morphologies of synthesized materials.

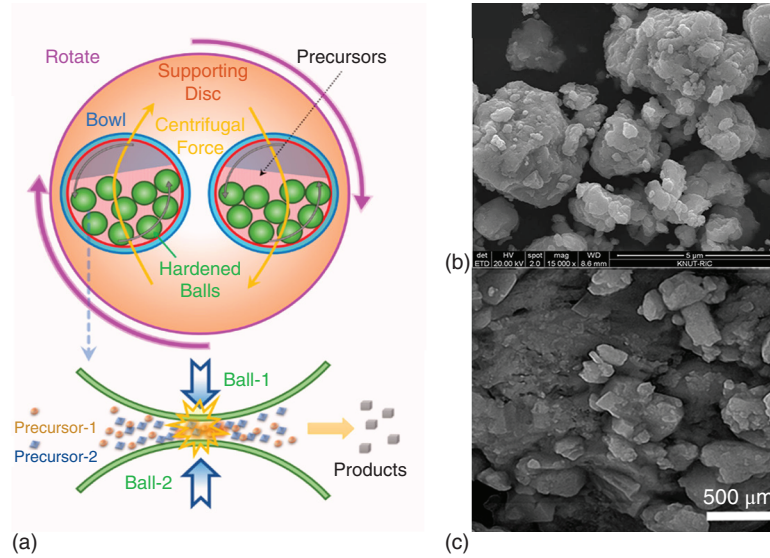


**Figure 1.10** (a) Schematic diagram of mechanical alloying. Source: Reproduced with permission from Shi et al. [54]/American Chemical Society. Scanning electron microscope (SEM) images of FeVSb (b) and Bi<sub>2</sub>Te<sub>3</sub> (c) samples. Source: Reproduced with permission from Hasan and Ur [60]/Springer Nature.

In addition, the ball milling process is also a very common method in the preparation of thermoelectric materials, especially for high-temperature thermoelectric materials or elements that contain easily gasified elements. The schematic diagram of the ball milling process is shown (Figure 1.10a). Using this mechanical alloying process, here are FeV<sub>1-x</sub>Ti<sub>x</sub>Sb half-Heusler alloy successfully synthesized [60], and the scanning electron microscope (SEM) image of alloy powder (Figure 1.10b). Followed by hot pressing, powder fabricated by ball milling is transformed into dense bulk. Bi<sub>2</sub>Te<sub>3</sub> samples with the highest thermoelectric figure of merit at temperatures ranging from 573 to 673 K were synthesized using a combination of mechanical alloying [61] (Figure 1.10c). The half-Heusler Nb<sub>0.55</sub>Ta<sub>0.40</sub>Ti<sub>0.05</sub>FeSb alloyed by ball milling can approach a maximum power factor of 78 μW cm<sup>-1</sup> K<sup>-2</sup>, whose performance is much better than NbFeSb single crystal samples [17].

Solvothermal preparation is also a promising method for the synthesis of thermoelectric materials. This technique involves the use of solvents at elevated temperatures and pressures, allowing the precise control of the component, structure, and properties of as-synthesized materials. Solvothermal synthesis offers the ability to achieve uniform mixing and homogenization of constituents, which is beneficial to improving thermoelectric performance. With the solvothermal synthesis method, the controllable degree of particle size, shape, and distribution is heavily dependent on the solubility of precursors in solvents under the elevated temperature, and the high solubility of precursors can enhance the controllable degree of particle size, shape, and distribution, thereby improving the thermoelectric properties of as-synthesized materials. Furthermore, solvothermal synthesis

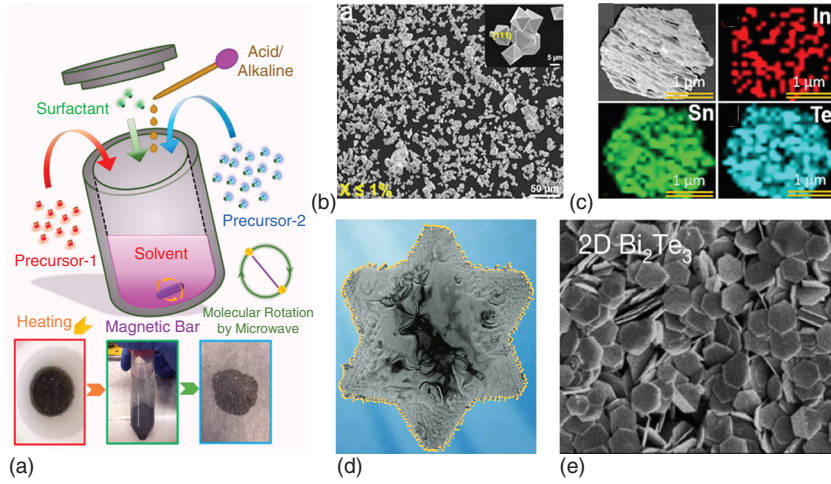


**Figure 1.11** (a) Schematic diagram of the solvothermal synthesis process, (b) images of SnTe microcrystal, and (c) energy dispersive spectrometer (EDS) maps for prepared SnTe microcrystal. Sb<sub>2</sub>Te<sub>3</sub> nanoplate (d), and Bi<sub>2</sub>Te<sub>3</sub> nanoparticle (e) using solvothermal synthesis. Sources: (a) Reproduced with permission from Shi et al. [54]/American Chemical Society. (b and c) Reproduced with permission from Moshwan et al. [62]/American Chemical Society. (d) Reproduced with permission from Dun et al. [63]/John Wiley & Sons. (e) Zeng et al. [64]/Springer Nature/CC BY 4.0.

enables the incorporation of dopants or the formation of composites, providing opportunities to tailor the properties of thermoelectric materials. With ongoing research and advancements in solvothermal techniques, this method holds great promise for the development of high-performance thermoelectric materials. The schematic diagram of the solvothermal principle is shown (Figure 1.11a). The microcrystal SnTe synthesized by solvothermal method [62] (Figure 1.11b). Synthesis quality was demonstrated by the energy dispersive spectrometer (EDS) characterization (Figure 1.11c). At 773 K, Sn<sub>0.99</sub>In<sub>0.01</sub>Te exhibits an impressive power factor of  $\sim 21.8 \mu\text{W cm}^{-1} \text{K}^{-2}$ , and concurrently achieves a  $ZT$  value of  $\sim 0.78$  [62]. The solvothermal method is well suited to the synthesis of nanostructured thermoelectric materials. The Sb<sub>2</sub>Te<sub>3</sub> nanoplate was fabricated by the solvothermal method [63] (Figure 1.11d). 2D bismuth telluride nanosheets were also synthesized by this method and used as raw material for the high-throughput airgel 3D printing [64] (Figure 1.11e).

3D printing, also known as additive manufacturing, allows for the precise layer-by-layer deposition of materials, enabling the creation of complex geometries and intricate structures. Thus, it is also regarded as a promising approach for the fabrication of thermoelectric materials. By utilizing 3D printing, researchers can personalize the design of thermoelectric devices, optimizing their efficiency and performance. Additionally, 3D printing offers the advantages of reduced material waste and the ability to create intricate thermoelectric architectures, which is difficult to achieve through traditional fabrication methods. Various thermoelectric materials, including semiconductors and composites, have been successfully

printed by the fused deposition modeling (FDM), selective laser sintering (SLS), and inkjet printing methods. However, challenges still exist, such as the limited availability of suitable thermoelectric inks and the unsatisfactory thermoelectric properties of printed materials. Nevertheless, the rapid progress in 3D printing technology and raw printing materials still hold great promise for the development of highly efficient and customizable thermoelectric devices in the future.

Research on 3D printing synthetic thermoelectric materials is just getting started. The schematic diagram of printing synthetic thermoelectric materials is shown (Figure 1.12a) [65]. The elemental powders were first placed into a powder bed, and then a fiber laser was employed to melt these powders and printed alloys. In the whole process, each alloyed layer was melted twice by the fiber laser to form dense thermoelectric ingots under a high-purity argon environment. In the selective laser melting (SLM) process, a mixture of Sb and Te elemental powders is utilized as the initial materials. The printed sample and its morphology of  $\text{Sb}_2\text{Te}_3$  have been given (Figure 1.12f,g) [65]. When a blend of Bi and Te elemental powders is utilized

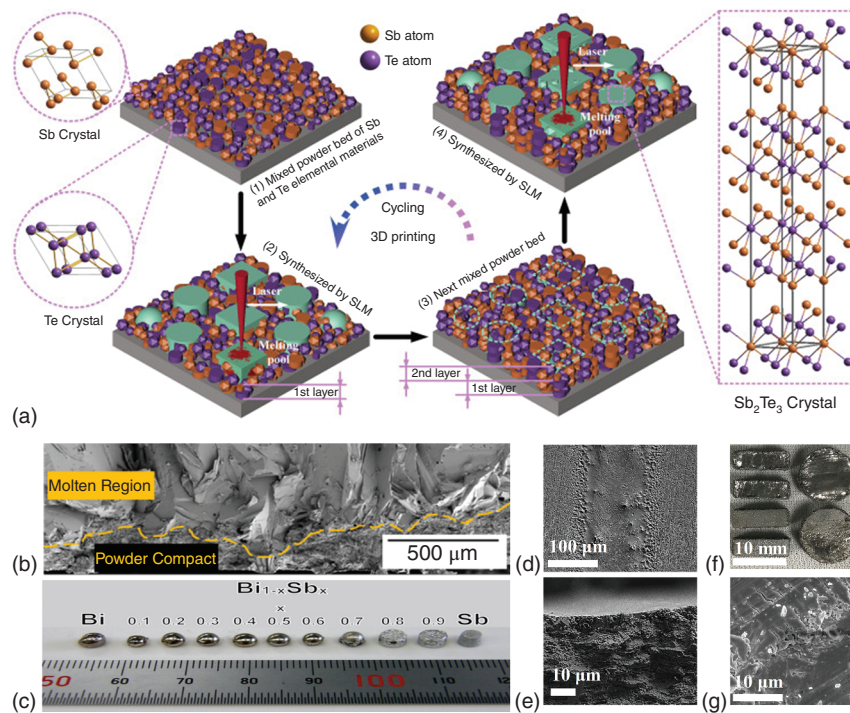


**Figure 1.12** (a) Schematic diagram of printing synthesis. Source: Reproduced with permission from Shi et al. [65]/ELSEVIER. (b) Cross-section of  $\text{Bi}_2\text{Te}_3$  molten region. Source: Reproduced with permission from El-Desouky et al. [66]/ELSEVIER. (c) Photo of  $\text{Bi}_{1-x}\text{Sb}_x$  samples synthesized by laser printing, and melt line on a bismuth telluride (d) and its cross-section (e), and photo (f) and SEM image (g) of  $\text{Sb}_2\text{Te}_3$  sample. Sources: (c) Reproduced with permission from Kinemuchi et al. [67]/ELSEVIER. (d and e) Reproduced with permission from El-Desouky et al. [68]/ELSEVIER. (f and g) Reproduced with permission from Shi et al. [65]/ELSEVIER.

as the initial materials, the morphology of the molten pool for  $\text{Bi}_2\text{Te}_3$  specimens is reported (Figure 1.12b), indicating the feasibility of printing [66]. Thermoelectric compounds, including alloys, intermetallic compounds, and oxides, have been successfully synthesized using laser melting (Figure 1.12c) [67]. The morphology and cross-section of the single-pass melt pool of laser printed bismuth telluride are presented (Figure 1.12d,e) [68], suggesting that suitable laser printing parameters can form good surface features.

## 1.5 Thermoelectric Devices and Their Applications

### 1.5.1 Conventional Devices

In a thermoelectric module, a metal electrode is required to connect the p- and n-type thermoelectric materials. To elevate the performance of thermoelectric modules, the type of metal electrode and thermoelectric materials can be chosen optimally, thereby manipulating the contact resistance between them to obtain a better output voltage. However, the output voltage of single thermoelectric module is still low, thus it is necessary to connect several thermoelectric modules in parallel or in series and form a thermoelectric device.

According to geometrical structure, conventional thermoelectric devices are divided into three types:  $\pi$ -, O- and Y-type [54] (Figure 1.13). Among them, the  $\pi$ -type thermoelectric device, integrating modules into two plates with large thermal conductivity and electrical insulation, is the mostly frequently-used. In the  $\pi$ -type thermoelectric device, heat flow transmits along the axis perpendicular to the two plates, suitable for working environments with flat heat sources. However, the hot (top) and cold (bottom) surfaces are usually constrained in the  $\pi$ -type thermoelectric device, which results in a vertical temperature difference. Due to the existence of thermal expansion difference, this vertical temperature difference is likely to cause considerable thermal strain, thereby damagins the device reliability. In the O-type thermoelectric device, n- and p-type thermoelectric materials are arranged in alternating coaxial with cylindrical heat sources. To realize the electrical insulation between adjacent thermoelectric materials, annular insulation materials are

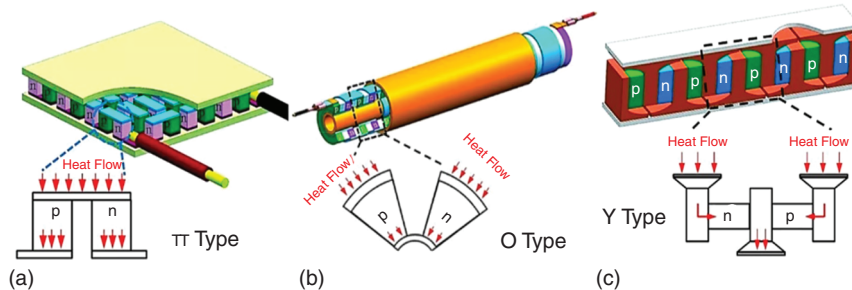


**Figure 1.13** Diagram of  $\pi$ - (a), O- (b) and Y-type (c) thermoelectric devices.  
Source: Reproduced with permission from Shi et al. [54]/American Chemical Society.

employed and placed between each thermoelectric material layer. Meantime, the metal electrodes are also employed to connect adjacent thermoelectric materials. Compared to the  $\pi$ -type thermoelectric device, the O-type thermoelectric device is more suitable for working environments with a non-flat heat source. However, the manufacturing cost of O-type thermoelectric devices is much higher than the  $\pi$ -type. Because the soldering between special shaped thermoelectric materials and metal electrodes, as well as the integration technology of devices, are more difficult than flat devices. In the Y-type thermoelectric device, each n- or p-type thermoelectric material is sandwiched between electrode plates (Figure 1.13c). Based on this unique structure, each electrode plate not only provides conductive paths between adjacent p-type and n-type thermoelectric materials, but also serves as collector and heat transfer components.

The shape of thermoelectric materials can be rectangular or cylindrical. Compared to the  $\pi$ - and O-type thermoelectric devices, the lateral series in a Y-type thermoelectric device can eliminate the stress induced by the difference in thermal expansion coefficients of p-type and n-type thermoelectric materials significantly. Furthermore, each thermoelectric module in Y-type structures is allowed to be optimized independently, which is beneficial to the manufacture of segmented structures. However, there are two main concerns in designing the conventional thermoelectric device. One is the choice of thermoelectric materials with robust mechanical properties and high thermoelectric performance, while another concern is how to connect the thermoelectric materials and electrodes. The appropriate selection of thermoelectric and interlayer materials can maintain the high performance of thermoelectric devices for a long time with high stability. With the development of the internet of things (IoT), more and more systems are connected by a network of billions of smart sensors. As a result, knowing how to power these smart sensors becomes an urgent problem to be solved. Thermoelectric energy conversion provides a possible solution to this problem. In particular, micro and flexible thermoelectric devices are required for the wireless sensor networks used for animal tracking and human health monitoring. Hence, researchers are beginning to design and manufacture miniaturized and flexible thermoelectric devices.

### 1.5.2 Miniature Devices

Although the fabrication techniques of miniature thermoelectric devices are complicated and the performance of miniature thermoelectric devices is lower than their conventional counterparts, they can use the temperature gradient in the ambient environment to generate electricity and realize an in-situ power supply for the micro electro-mechanical systems (MEMS) and the smart sensors in IoT. According to their geometrical structure, miniature thermoelectric devices are classified into three types: vertical, lateral, and hybrid (Figure 1.14).

In the vertical miniature thermoelectric devices, the arrangement of thermoelectric materials is perpendicular to the substrate, and then the heat flow transmits vertically across the thermoelectric materials [69] (Figure 1.14a). In 1999, Kishi

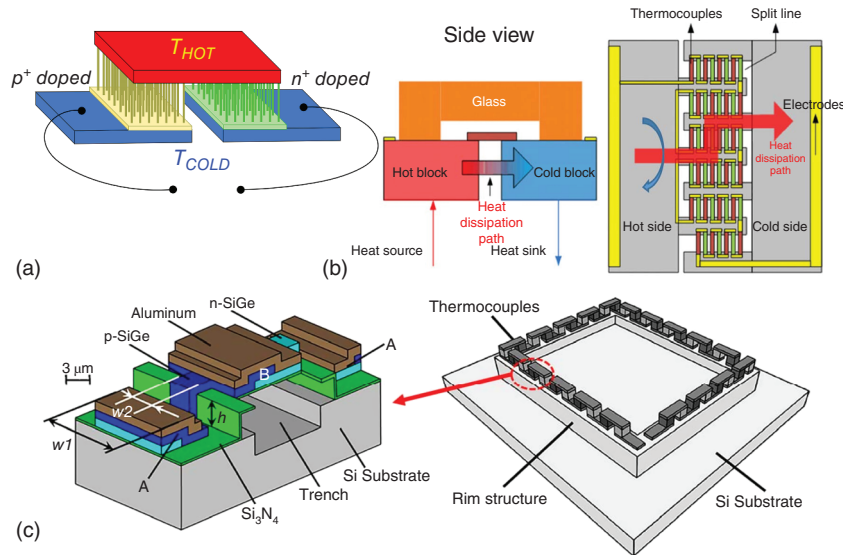


**Figure 1.14** Structure of the vertical (a), lateral (b) and hybrid (c) miniature thermoelectric devices. Source: (a) Elyamny et al. [69]/American Chemical Society/CC BY4.0. (b) Reproduced with permission from Yu et al. [70]/IOP Publishing. (c) Reproduced with permission from Wang et al. [71]/ELSEVIER.

et al. [72] were the first to manufacture a vertical miniature thermoelectric device and used it to power wristwatch. Subsequently, Snyder et al. [73] and Li et al. [74] also fabricated vertical miniature thermoelectric devices through MEMS-like electrochemical process and combined MEMS technology and materials processing, respectively. With the development of micropelt platform technology,  $\sim 8000$  p-n couples per  $\text{cm}^2$  could be achieved by 2007, and the open circuit voltage and maximum power output can be up to 2.3 V and 2.8 mW at temperature difference of 10 K [75]. Li et al. [76] fabricated a chip-level vertical miniature thermoelectric generator based on Si nanowire array, where the Si nanowire array were prepared by top-down complementary metal oxide semiconductor (CMOS) technology. The size of this generator is  $5 \times 5 \text{ mm}^2$ , and the output power is 1.5 nW under temperature difference of 0.12 K across the Si nanowire.

In lateral miniature thermoelectric devices, there are in-plane thermopile (Figure 1.14b) [70], and then the heat flows along the horizontal direction perpendicularly to the thermoelectric materials. Kiely et al. [77] were the first to present the design of a lateral miniature thermoelectric device whose output power reached 20 pW with the voltage off  $\sim 4.0$  V. In the design by Stordeur et al., the thermoelectric device consists of 70 segments connected in series. Glosch et al. [78] fabricated a lateral miniature thermoelectric device using silicon technology, and realized an output power of 1.5 mW under 10 K temperature difference. Yu et al. [70] reported a CMOS-based lateral structure with horizontal dissipation path (Figure 1.14b). To reduce the thermal contact resistance further, they etched the silicon substrate into two comb-shaped blocks used as thermally isolated



hot and cool ends of an individual micro thermoelectric device. The size of an individual micro thermoelectric device is  $3 \times 3 \text{ mm}^2$  and its output voltage can be up to  $146 \text{ mV K}^{-1}$ .

In 2009, Wang et al. realized a micro thermoelectric device with hybrid structure for human body applications [71] (Figure 1.14c). In their design, a trench with a depth of  $2.5 \text{ }\mu\text{m}$  was formed below the cold junction, while an extra step with a height of  $0.5 \text{ }\mu\text{m}$  was made on the top of the trench. Then, to reduce the contact resistance, they reduced the width of the thermocouple leg to the technological limit, when the width of the junction area remained large. Furthermore, a rim structure was formed by deep reaction-ion etching (DRIE) of Si substrate. The open-circuit output voltage was measured as  $12.5 \text{ V cm}^{-2} \text{ K}^{-1}$  on matched external load, and the corresponding power was up to  $0.026 \text{ }\mu\text{W cm}^{-2} \text{ K}^{-1}$ . In 2010, Xie et al. [79] proposed a CMOS MEMS-based hybrid micro thermoelectric device by making cavities, and the open-circuit voltage and output power can reach  $16.7 \text{ V}$  and  $1.3 \text{ }\mu\text{W cm}^{-2}$  on matched external load under a temperature difference of  $5 \text{ K}$ , respectively. Ziouche et al. [80] elevated the output power of hybrid micro thermoelectric device to  $12.3 \text{ }\mu\text{W cm}^{-2}$  by designing a silicon-based monolithic planar thermoelectric device, which can be fabricated by bonding technology. In their design, the air cavities in Si wafers were created by a back-side DRIE process. To protect the membranes from pressure, the oxidized porous-Si was employed in the bonding process.

### 1.5.3 Flexible Devices

Compared with traditional thermoelectric devices, not only the high thermoelectric performance and excellent stability, but also the certain flexibility without structural damage, are required in flexible thermoelectric devices to power wearable electronic devices. In recent years, many advanced fabrication methods of flexible thermoelectric devices have been proposed and developed. In 2019, Burton et al. [81] reported a flexible thermoelectric device by employing Cu metal to connect the thermoelectric units manufactured from 3D-printed SnSe (Figure 1.15a). The 3D-printing process, involving the production of a 3D object from the design model by successively adding materials layer-by-layer, is a powerful tool to fabricate miniature thermoelectric devices. In Burton's design, the 3D-printed bulk SnSe material displays a high figure of merit of 1.7 at  $758 \text{ K}$ , suggesting a high performance. The flexibility in their device benefits from the Cu tape as electrode and interconnectors, while the output power of this device is larger than  $20 \text{ }\mu\text{W}$ . Inspired by this design, Singh et al. [82] used the Au-coated Cu as a connector and designed a lightweight device with eight pairs of thermoelectric units, and realized an output power of  $5 \text{ }\mu\text{W}$ . Their thermoelectric unit is based on the strain-induced self-rolling  $\text{Sb}_2\text{Te}_3$  and  $\text{Bi}_2\text{Te}_3$  films.

Compared with the Au and Cu interconnectors, organic substrates possess several unique advantages, such as high cost-effectiveness, high bending fatigue strength, and multiple choices for various purposes. Meantime, the existence of organic substrates can provide effective protection for electrode and inorganic thermoelectric materials from mechanical shock and oxidation. Therefore inducing the

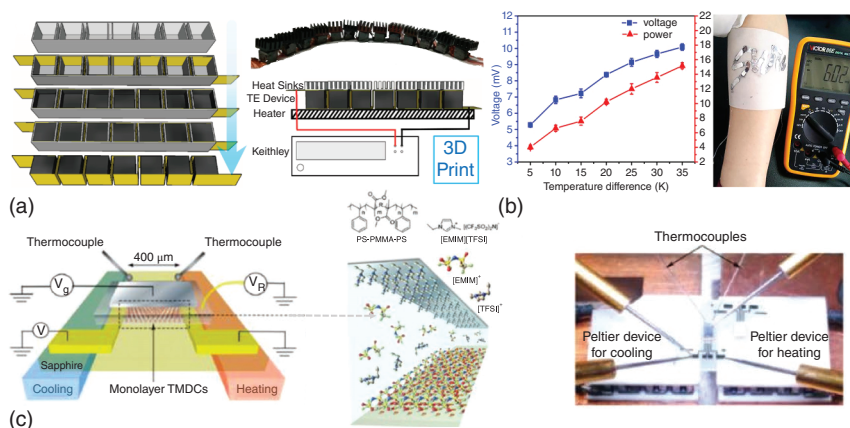


**Figure 1.15** (a) Schematic diagram and optical image of fabricating chain-like thermoelectric devices by 3D-printing. Source: Burton et al. [81]/John Wiley & Sons/CC BY 4.0. (b) Photo and output voltage of the glass fabric-based thermoelectric device. Source: Reproduced with permission from Lu et al. [83]/ELSEVIER. (c) Diagram and optical image of MoS<sub>2</sub>/WSe<sub>2</sub> flexible thermoelectric device. Source: Reproduced with permission from Pu et al. [84]/American Physical Society.

organic substrates is also an advanced method to fabricate flexible thermoelectric devices. In 2016, Lu et al. [83] reported a thermoelectric generator based on the nanostructure Bi<sub>2</sub>Te<sub>3</sub> and Sb<sub>2</sub>Te<sub>3</sub>, while Bi<sub>2</sub>Te<sub>3</sub> and Sb<sub>2</sub>Te<sub>3</sub> were deposited on both sides of silk fabric to harvest energy from people walking. Due to its excellent flexibility, it can be attached to the arm (Figure 1.15b). The output voltage and power were measured to be 10 mV and 15 nW with a 35 K temperature difference. Kim et al. [85] proposed a glass fabric-based thermoelectric device, in which the inorganic thermoelectric materials were connected by Cu electrodes and fixed in a flexible polydimethylsiloxane (PDMS) substrate. The open-circuit output voltage and the output power of their design is up to 85 mV and 11 400 μW at a temperature difference of 47.5 K. In these flexible thermoelectric devices, all of the inorganic thermoelectric materials are bulk. In 2004, graphene with ultra-high Young's moduli and excellent fracture strength was successfully peeled off by mechanical exfoliation, which prompted the study of 2D materials. Compared with bulk materials, 2D materials possess admirable ductility, which is more suitable for flexible devices. Furthermore, it has been reported that the largest power factor for bilayer MoS<sub>2</sub> is up to 8500 μW cm<sup>-1</sup> K<sup>-2</sup> due to the 2D confinement effect, the large effective carrier mass, and valley degeneracies in MoS<sub>2</sub>, thus making TMDs promising candidates for nanosized flexible thermoelectric devices [26]. In 2016, Pu et al. [84] fabricated several flexible thermoelectric devices based on large-area MoS<sub>2</sub> and WSe<sub>2</sub> thin films, while the MoS<sub>2</sub> and WSe<sub>2</sub> thin films were obtained through chemical vapor deposition growth. In their design, SiO<sub>2</sub> was used as back and gate substrates, and a transistor structure was established (Figure 1.15c). To enhance the intrinsic thermoelectric performance of MoS<sub>2</sub> and WSe<sub>2</sub> thin films, ion gels and gelled ionic liquids were introduced as electrolytes. Compared to the pristine



MoS<sub>2</sub> and WSe<sub>2</sub> thin films, the ion gelngoffer high carrier density accumulation, and make the thermoelectric transistor exhibng an improved transport properties. The optimized Seebeck coefficient reached 160  $\mu\text{V K}^{-1}$ , while the output power was up to 200  $\mu\text{W cm}^{-1} \text{K}^{-1}$ .

## 1.6 Conclusions and Outlook

In recent years, thermoelectric materials have developed rapidly, and many thermoelectric materials with excellent performance have been designed and prepared for waste heat energy recovery and supply to electronic devices. In this section, we introduced the principles of thermoelectric conversion technology, various frequently used thermoelectric materials, the preparation and forming processes of thermoelectric materials, as well as thermoelectric devices. Here, we also provide an outlook on the development of thermoelectric technology in future. Firstly, although the figure of merit in thermoelectric materials and the conversion efficiency of thermoelectric devices have been greatly improved, the widespread application of thermoelectric technology still requires a wide range of raw materials with good processability, excellent performance, and stability. Secondly, half-Heusler alloy with good machinability and excellent thermal stability is one of the potential materials suitable for large-scale commercial applications.

However, compared to other thermoelectric materials, half-Heusler alloy has a higher lattice thermal conductivity, forming an obstacle to the application of half-Heusler alloy in thermoelectric conversion. With the development of additive manufacturing technology, controllable nanostructures may provide new electrothermal decoupling mechanisms, which offers a possible route to decrease the lattice thermal conductivity. Furthermore, the rapid development of additive manufacturing, especially multi material additive manufacturing, provides new solutions for the integrated manufacturing of complex thermoelectric devices and interface failure problems, which is beneficial for the improvement of device conversion efficiency.

## Acknowledgment

This work was supported by the National Natural Science Foundation of China (No. 12204373).

## References

- 1 Jaziri, N., Boughamoura, A., Müller, J. et al. (2020). A comprehensive review of thermoelectric generators: technologies and common applications. *Energy Reports* 6: 264–287.
- 2 Yu, Y., Cagnoni, M., Cojocaru-Mirédin, O., and Wuttig, M. (2020). Chalco-genide thermoelectrics empowered by an unconventional bonding mechanism. *Advanced Functional Materials* 30: 1904862.

- 3 Zhuang, H.-L., Pan, Y., Sun, F.-H. et al. (2019). Thermoelectric Cu-doped  $(\text{Bi,Sb})_2\text{Te}_3$ : performance enhancement and stability against high electric current pulse. *Nano Energy* 60: 857–865.
- 4 Mao, J., Liu, Z., Zhou, J. et al. (2018). Advances in thermoelectrics. *Advances in Physics* 67: 69–147.
- 5 Tsai, Y.-F., Wei, P.-C., Chang, L. et al. (2021). Compositional fluctuations locked by athermal transformation yielding high thermoelectric performance in GeTe. *Advanced Materials* 33: 2005612.
- 6 Hong, M., Zou, J., and Chen, Z.-G. (2019). Thermoelectric GeTe with diverse degrees of freedom having secured superhigh performance. *Advanced Materials* 31: 1807071.
- 7 Kim, H.-S., Dharmaiyah, P., Madavali, B. et al. (2017). Large-scale production of  $(\text{GeTe})_x(\text{AgSbTe}_2)_{100-x}$  ( $x=75, 80, 85, 90$ ) with enhanced thermoelectric properties via gas-atomization and spark plasma sintering. *Acta Materialia* 128: 43–53.
- 8 Hong, M., Li, M., Wang, Y. et al. (2023). Advances in versatile GeTe thermoelectrics from materials to devices. *Advanced Materials* 35: 2208272.
- 9 Chang, C. and Kanatzidis, M.G. (2022). High-entropy thermoelectric materials emerging. *Materials Lab* 1: 220048.
- 10 Jiang, B., Wang, W., Liu, S. et al. (2022). High figure-of-merit and power generation in high-entropy GeTe-based thermoelectrics. *Science* 377: 208–213.
- 11 Goldsmid, H.J. and Douglas, R.W. (1954). The use of semiconductors in thermoelectric refrigeration. *British Journal of Applied Physics* 5: 386.
- 12 Lu, Y., Zhou, Y., Wang, W. et al. (2023). Staggered-layer-boosted flexible  $\text{Bi}_2\text{Te}_3$  films with high thermoelectric performance. *Nature Nanotechnology* 18: 1281–1288.
- 13 Poudel, B., Hao, Q., Ma, Y. et al. (2008). High-thermoelectric performance of nanostructured bismuth antimony telluride bulk alloys. *Science* 320: 634–638.
- 14 Garmroudi, F., Parzer, M., Riss, A. et al. (2022). Anderson transition in stoichiometric  $\text{Fe}_2\text{VAl}$ : high thermoelectric performance from impurity bands. *Nature Communications* 13: 3599.
- 15 Hinterleitner, B., Knapp, I., Poneder, M. et al. (2019). Thermoelectric performance of a metastable thin-film Heusler alloy. *Nature* 576: 85–90.
- 16 Zeier, W.G., Schmitt, J., Hautier, G. et al. (2016). Engineering half-Heusler thermoelectric materials using Zintl chemistry. *Nature Reviews Materials* 1: 16032.
- 17 Zhu, H., Li, W., Nozariasbmarz, A. et al. (2023). Half-Heusler alloys as emerging high power density thermoelectric cooling materials. *Nature Communications* 14: 3300.
- 18 Ren, W., Xue, W., Guo, S. et al. (2023). Vacancy-mediated anomalous phononic and electronic transport in defective half-Heusler  $\text{ZrNiBi}$ . *Nature Communications* 14: 4722.
- 19 Li, W., Yang, G., and Zhang, J. (2016). Optimization of the thermoelectric properties of  $\text{FeNbSb}$ -based half-Heusler materials. *Journal of Physics D: Applied Physics* 49: 195601.
- 20 Li, D., Gong, Y., Chen, Y. et al. (2020). Recent progress of two-dimensional thermoelectric materials. *Nano-Micro Letters* 12: 36.

- 21 Suh, J., Yu, K.M., Fu, D. et al. (2015). Simultaneous enhancement of electrical conductivity and thermopower of  $\text{Bi}_2\text{Te}_3$  by multifunctionality of native defects. *Advanced Materials* 27: 3681–3686.
- 22 Gu, X., Li, B., and Yang, R. (2016). Layer thickness-dependent phonon properties and thermal conductivity of  $\text{MoS}_2$ . *Journal of Applied Physics* 119: 085106.
- 23 Xu, K., Gabourie, A.J., Hashemi, A. et al. (2019). Thermal transport in  $\text{MoS}_2$  from molecular dynamics using different empirical potentials. *Physical Review B* 99: 054303.
- 24 Yoon, Y., Ganapathi, K., and Salahuddin, S. (2011). How good can monolayer  $\text{MoS}_2$  transistors be? *Nano Letters* 11: 3768–3773.
- 25 Kayyalha, M., Maassen, J., Lundstrom, M. et al. (2016). Gate-tunable and thickness-dependent electronic and thermoelectric transport in few-layer  $\text{MoS}_2$ . *Journal of Applied Physics* 120: 134305.
- 26 Hippalgaonkar, K., Wang, Y., Ye, Y. et al. (2017). High thermoelectric power factor in two-dimensional crystals of  $\text{MoS}_2$ . *Physical Review B* 95: 115407.
- 27 Jiang, P., Qian, X., Gu, X., and Yang, R. (2017). Probing anisotropic thermal conductivity of transition metal dichalcogenides  $\text{MX}_2$  ( $M = \text{Mo}, \text{W}$  and  $X = \text{S}, \text{Se}$ ) using time-domain thermoreflectance. *Advanced Materials* 29: 1701068.
- 28 Li, L., Yu, Y., Ye, G.J. et al. (2014). Black phosphorus field-effect transistors. *Nature Nanotechnology* 9: 372–377.
- 29 Lee, S., Yang, F., Suh, J. et al. (2015). Anisotropic in-plane thermal conductivity of black phosphorus nanoribbons at temperatures higher than 100 K. *Nature Communications* 6: 8573.
- 30 Luo, Z., Maassen, J., Deng, Y. et al. (2015). Anisotropic in-plane thermal conductivity observed in few-layer black phosphorus. *Nature Communications* 6: 8572.
- 31 Qin, G., Yan, Q.-B., Qin, Z. et al. (2015). Anisotropic intrinsic lattice thermal conductivity of phosphorene from first principles. *Physical Chemistry Chemical Physics* 17: 4854–4858.
- 32 Liu, H., Choe, H.S., Chen, Y. et al. (2017). Variable range hopping electric and thermoelectric transport in anisotropic black phosphorus. *Applied Physics Letters* 111: 102101.
- 33 Ding, G., Hu, Y., Li, D., and Wang, X. (2019). A comparative study of thermoelectric properties between bulk and monolayer  $\text{SnSe}$ . *Results in Physics* 15: 102631.
- 34 Guo, R., Wang, X., Kuang, Y., and Huang, B. (2015). First-principles study of anisotropic thermoelectric transport properties of IV-VI semiconductor compounds  $\text{SnSe}$  and  $\text{SnS}$ . *Physical Review B* 92: 115202.
- 35 Zhou, C., Lee, Y.K., Yu, Y. et al. (2021). Polycrystalline  $\text{SnSe}$  with a thermoelectric figure of merit greater than the single crystal. *Nature Materials* 20: 1378–1384.
- 36 Sun, Y., Shuai, Z., and Wang, D. (2019). Reducing lattice thermal conductivity of the thermoelectric  $\text{SnSe}$  monolayer: role of phonon–electron coupling. *The Journal of Physical Chemistry C* 123: 12001–12006.
- 37 Khazaei, M., Arai, M., Sasaki, T. et al. (2014). Two-dimensional molybdenum carbides: potential thermoelectric materials of the MXene family. *Physical Chemistry Chemical Physics* 16: 7841–7849.

- 38 Kim, H., Anasori, B., Gogotsi, Y., and Alshareef, H.N. (2017). Thermoelectric properties of two-dimensional molybdenum-based MXenes. *Chemistry of Materials* 29: 6472–6479.
- 39 Xu, Q., Wan, Y., Hu, T.S. et al. (2015). Robust self-cleaning and micromanipulation capabilities of gecko spatulae and their bio-mimics. *Nature Communications* 6: 8949.
- 40 Zhao, Y., Zheng, M., Wu, J. et al. (2021). Modification of thermal transport in few-layer MoS<sub>2</sub> by atomic-level defect engineering. *Nanoscale* 13: 11561–11567.
- 41 Sharma, M., Kumar, A., and Ahluwalia, P.K. (2019). Electron transport and thermoelectric performance of defected monolayer MoS<sub>2</sub>. *Physica E: Low-dimensional Systems and Nanostructures* 107: 117–123.
- 42 Yu, C., Zhang, G., Zhang, Y.-W., and Peng, L.-M. (2015). Strain engineering on the thermal conductivity and heat flux of thermoelectric Bi<sub>2</sub>Te<sub>3</sub> nanofilm. *Nano Energy* 17: 104–110.
- 43 Zhang, G. and Zhang, Y.-W. (2015). Strain effects on thermoelectric properties of two-dimensional materials. *Mechanics of Materials* 91: 382–398.
- 44 Ding, G., He, J., Gao, G.Y., and Yao, K. (2018). Two-dimensional MoS<sub>2</sub>-MoSe<sub>2</sub> lateral superlattice with minimized lattice thermal conductivity. *Journal of Applied Physics* 124: 165101.
- 45 Wang, S., Yang, X., Hou, L. et al. (2022). Organic covalent modification to improve thermoelectric properties of TaS<sub>2</sub>. *Nature Communications* 13: 4401.
- 46 Balandin, A.A., Ghosh, S., Bao, W. et al. (2008). Superior thermal conductivity of single-layer graphene. *Nano Letters* 8: 902–907.
- 47 Ghosh, S., Calizo, I., Teweldebrhan, D. et al. (2008). Extremely high thermal conductivity of graphene: prospects for thermal management applications in nanoelectronic circuits. *Applied Physics Letters* 92: 151911.
- 48 Seol, J.H., Moore, A.L., Shi, L. et al. (2010). Thermal conductivity measurement of graphene exfoliated on silicon dioxide. *Journal of Heat Transfer* 133: 022403.
- 49 He, M., Zhao, Y., Wang, B. et al. (2015). 3D printing fabrication of amorphous thermoelectric materials with ultralow thermal conductivity. *Small* 11: 5889–5894.
- 50 Chen, B., Das, S.R., Zheng, W. et al. (2017). Inkjet printing of single-crystalline Bi<sub>2</sub>Te<sub>3</sub> thermoelectric nanowire networks. *Advanced Electronic Materials* 3: 1600524.
- 51 Yang, S.E., Kim, F., Ejaz, F. et al. (2021). Composition-segmented BiSbTe thermoelectric generator fabricated by multimaterial 3D printing. *Nano Energy* 81: 105638.
- 52 Park, S.H., Jo, S., Kwon, B. et al. (2016). High-performance shape-engineerable thermoelectric painting. *Nature Communications* 7: 13403.
- 53 Kim, F., Kwon, B., Eom, Y. et al. (2018). 3D printing of shape-conformable thermoelectric materials using all-inorganic Bi<sub>2</sub>Te<sub>3</sub>-based inks. *Nature Energy* 3: 301–309.
- 54 Shi, X.-L., Zou, J., and Chen, Z.-G. (2020). Advanced thermoelectric design: from materials and structures to devices. *Chemical Reviews* 120: 7399–7515.

- 55 Duong, A.T., Nguyen, V.Q., Duvjir, G. et al. (2016). Achieving  $ZT=2.2$  with Bi-doped n-type SnSe single crystals. *Nature Communications* 7: 13713.
- 56 Wang, Q.-Q., Liu, K.-F., Su, Y.-Y. et al. (2023). High thermoelectric performance and anisotropy studies of n-type  $Mg_3Bi_2$ -based single crystal. *Acta Materialia* 255: 119028.
- 57 Jin, M., Jiang, J., Li, R. et al. (2019). Growth of large size SnSe single crystal and comparison of its thermoelectric property with polycrystal. *Materials Research Bulletin* 114: 156–160.
- 58 Lee, K.H. and Kim, S.W. (2017). Design and preparation of high-performance bulk thermoelectric materials with defect structures. *Journal of the Korean Ceramic Society* 54: 75–85.
- 59 Aversano, F., Ferrario, A., Boldrini, S. et al. (2018). Thermoelectric properties of TiNiSn half Heusler alloy obtained by rapid solidification and sintering. *Journal of Materials Engineering and Performance* 27: 6306–6313.
- 60 Hasan, R. and Ur, S.-C. (2018). Thermoelectric and transport properties of  $FeV_{1-x}Ti_xSb$  half-Heusler system synthesized by controlled mechanical alloying process. *Electronic Materials Letters* 14: 725–732.
- 61 Bolghanabadi, N., Sajjadi, S.A., Babakhani, A., and Saberi, Y. (2021). Effects of synthesis parameters and thickness on thermoelectric properties of  $Bi_2Te_3$  fabricated using mechanical alloying and spark plasma sintering. *Journal of Electronic Materials* 50: 1331–1339.
- 62 Moshwan, R., Shi, X.-L., Liu, W.-D. et al. (2019). Enhancing thermoelectric properties of InTe nanoprecipitate-embedded  $Sn_{1-x}In_xTe$  microcrystals through anharmonicity and strain engineering. *ACS Applied Energy Materials* 2: 2965–2971.
- 63 Dun, C., Hewitt, C.A., Li, Q. et al. (2017). 2D chalcogenide nanoplate assemblies for thermoelectric applications. *Advanced Materials* 29: 1700070.
- 64 Zeng, M., Du, Y., Jiang, Q. et al. (2023). High-throughput printing of combinatorial materials from aerosols. *Nature* 617: 292–298.
- 65 Shi, J., Chen, X., Wang, W., and Chen, H. (2021). A new rapid synthesis of thermoelectric  $Sb_2Te_3$  ingots using selective laser melting 3D printing. *Materials Science in Semiconductor Processing* 123: 105551.
- 66 El-Desouky, A., Carter, M., Mahmoudi, M. et al. (2017). Influences of energy density on microstructure and consolidation of selective laser melted bismuth telluride thermoelectric powder. *Journal of Manufacturing Processes* 25: 411–417.
- 67 Kinemuchi, Y., Mikami, M., Terasaki, I., and Shin, W. (2016). Rapid synthesis of thermoelectric compounds by laser melting. *Materials & Design* 106: 30–36.
- 68 El-Desouky, A., Carter, M., Andre, M.A. et al. (2016). Rapid processing and assembly of semiconductor thermoelectric materials for energy conversion devices. *Materials Letters* 185: 598–602.
- 69 Elyamny, S., Dimaggio, E., Magagna, S. et al. (2020). High power thermoelectric generator based on vertical silicon nanowires. *Nano Letters* 20: 4748–4753.
- 70 Yu, X., Wang, Y., Liu, Y. et al. (2012). CMOS MEMS-based thermoelectric generator with an efficient heat dissipation path. *Journal of Micromechanics and Microengineering* 22: 105011.

- 71 Wang, Z., Leonov, V., Fiorini, P., and Van Hoof, C. (2009). Realization of a wearable miniaturized thermoelectric generator for human body applications. *Sensors and Actuators A: Physical* 156: 95–102.
- 72 Kishi, M., Nemoto, H., Hamao, T. et al. (1999). *Proceedings of the Eighteenth International Conference on Thermoelectrics., ICT'99* (Cat. No.99TH8407), 301–307.
- 73 Snyder, G.J., Lim, J.R., Huang, C.-K., and Fleurial, J.-P. (2003). Thermoelectric microdevice fabricated by a MEMS-like electrochemical process. *Nature Materials* 2: 528–531.
- 74 Li, J.-F., Tanaka, S., Umeki, T. et al. (2003). Microfabrication of thermoelectric materials by silicon molding process. *Sensors and Actuators A: Physical* 108: 97–102.
- 75 Bottner, H., Nurnus, J., Schubert, A., and Volkert, F. (2007). *26th International Conference on Thermoelectrics*, 306–309.
- 76 Li, Y., Buddharaju, K., Singh, N. et al. (2011). Chip-level thermoelectric power generators based on high-density silicon nanowire array prepared with top-down CMOS technology. *IEEE Electron Device Letters* 32: 674–676.
- 77 Kiely, J.H. and Dong-Hi, L. (1997). Characteristics of thin-film thermoelectric devices for power generation. *Measurement Science and Technology* 8: 661.
- 78 Glosch, H., Ashauer, M., Pfeiffer, U., and Lang, W. (1999). A thermoelectric converter for energy supply. *Sensors and Actuators A: Physical* 74: 246–250.
- 79 Xie, J., Lee, C., and Feng, H. (2010). Design, fabrication, and characterization of CMOS MEMS-based thermoelectric power generators. *Journal of Microelectromechanical Systems* 19: 317–324.
- 80 Ziouche, K., Yuan, Z., Lejeune, P. et al. (2017). Silicon-based monolithic planar micro thermoelectric generator using bonding technology. *Journal of Microelectromechanical Systems* 26: 45–47.
- 81 Burton, M.R., Mehraban, S., Beynon, D. et al. (2019). 3D printed SnSe thermoelectric generators with high figure of merit. *Advanced Energy Materials* 9: 1900201.
- 82 Singh, D., Kutbee, A.T., Ghoneim, M.T. et al. (2018). Strain-induced rolled thin films for lightweight tubular thermoelectric generators. *Advanced Materials Technologies* 3: 1700192.
- 83 Lu, Z., Zhang, H., Mao, C., and Li, C.M. (2016). Silk fabric-based wearable thermoelectric generator for energy harvesting from the human body. *Applied Energy* 164: 57–63.
- 84 Pu, J., Kanahashi, K., Cuong, N.T. et al. (2016). Enhanced thermoelectric power in two-dimensional transition metal dichalcogenide monolayers. *Physical Review B* 94: 014312.
- 85 Kim, S.J., We, J.H., and Cho, B.J. (2014). A wearable thermoelectric generator fabricated on a glass fabric. *Energy & Environmental Science* 7: 1959–1965.

